

CALCIUM SILICATE PEROVSKITE'S SEISMIC VELOCITIES CAN EXPLAIN LLVPS IN EARTH'S LOWER MANTLE

A.R. Thomson^{1,2*}, W.A. Crichton², J.P. Brodholt^{1,3}, I.G. Wood¹, N.C. Siersch⁴, J. Muir⁵, D.P. Dobson¹ and Simon A. Hunt¹

¹Department of Earth Sciences, University College London, London, WC1E 6BT.

²ESRF - The European Synchrotron, 71 avenue des Martyrs, 38000 Grenoble, France.

³Centre for Earth Evolution and Dynamics, University of Oslo, N-0316 Oslo, Norway.

⁴Bayerisches Geoinstitut, University of Bayreuth, 95440 Bayreuth, Germany.

⁵School of Earth and Environment, University of Leeds, Leeds, LS2 9JT.

*Corresponding Author (a.r.thomson@ucl.ac.uk)

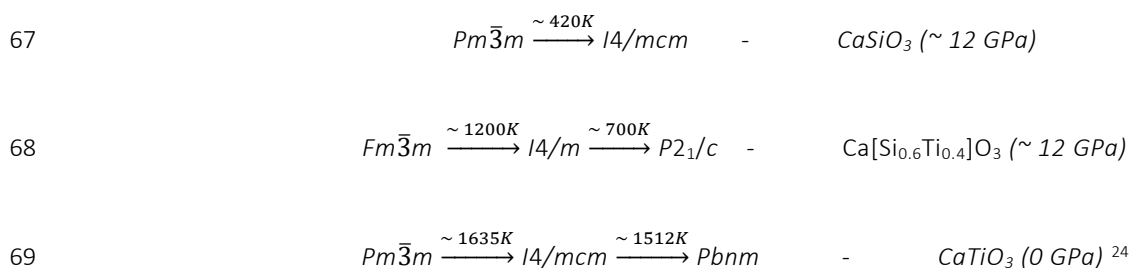
Seismology records the presence of various heterogeneities throughout the lower mantle^{e.g. 1,2}, however, the origins of these signals, whether thermal or chemical, remain uncertain and therefore much of the information they hold about the nature of the deep Earth is obscured. Accurate interpretation of observed velocities requires knowledge of the seismic properties of all of Earth's possible mineral components. Calcium silicate perovskite (hereafter "calcium perovskite") is believed to be the third most abundant mineral throughout the lower mantle. Here we measure the crystal structure, compressional and shear wave velocity of calcium perovskite samples, and provide direct constraints for calcium perovskite's adiabatic bulk and shear moduli. We observe that titanium incorporation into calcium perovskite stabilises the tetragonal structure to higher temperatures, and that the shear modulus of calcium perovskite is significantly lower than is predicted by computations³⁻⁵ or thermodynamic datasets⁶. When combined with literature data and extrapolated our results suggest subducted oceanic crust will be visible as low velocity anomalies throughout the lower mantle. In particular we show that large low-velocity provinces (LLVPs) are consistent with moderate enrichment of recycled oceanic crust, and mid-mantle discontinuities can be explained by a tetragonal-cubic phase transition in Ti-bearing calcium perovskite.

The lower mantle is vast, extending from the seismic discontinuity observed at ~ 660 km depth to the core-mantle boundary (CMB) at ~ 2890 km. Tomographic images demonstrate that despite a smooth variation of v_p , v_s and ρ in 1D velocity models the lower mantle is heterogeneous and regularly refertilised by subducting slabs^{7,8}. Sluggish diffusive re-equilibration and incomplete mechanical mixing^{e.g. 9} means that large-scale patterns of mantle convection may be directly observed via tomographic velocity anomalies and/or the distribution of seismic scatterers. Identifying the causes of heterogeneities requires accurate mineralogical models of Earth's mantle to facilitate comparisons between geophysical observations and predicted seismic velocities. However, a major uncertainty in many models^{e.g. 10,11} has been the influence of calcium silicate perovskite (capv, here corresponding to $\text{Ca}[\text{Si}_x\text{Ti}_{[1-x]}\text{O}_3]$) on velocity, despite the widespread expectation that it is the lower mantle's third most abundant phase comprising 5-10 and 24-29 vol.% of peridotitic¹² and basaltic¹³ assemblages respectively.

Uncertainties stem from a sparsity of reliable measurements of capv's physical properties, which are technically challenging because CaSiO_3 is unrecoverable¹⁴, undergoing spontaneous amorphisation at room temperature during decompression. The widely used thermodynamic model of Stixrude et al.⁶ predicts that capv is significantly faster than PREM¹⁵, and therefore slow velocity anomalies are difficult to explain using recycled crustal material. Whilst

38 this is the widely adopted view, there is currently no consensus on the seismic properties of capv. Existing high-*T*
 39 calculations³⁻⁵ suggest that capv might be either slightly slower or much faster than PREM¹⁵ (Figure 1). In contrast,
 40 room temperature experiments^{16,17} have measured a shear velocity of capv that is at least 7% slower than the lowest
 41 computational estimates; however there is difficulty extrapolating these to high-temperature conditions due to intervening
 42 phase transformations of the capv structure^{3,18,19}. Very recently, high-temperature experimental velocity measurements
 43 that are also slower than all computational values have been reported²⁰, although this study did not consider
 44 extrapolations of capv's velocity throughout the deep mantle, leaving capv's contribution in generating lower mantle
 45 signatures unresolved. Here we report synchrotron-based high *PT* experiments that simultaneously measure the
 46 crystal structure and seismic velocities (v_p and v_s) of $\text{Ca}[\text{Si}_x\text{Ti}_{1-x}]\text{O}_3$ compositions ($x=0.6$ and 1) that bracket the
 47 range of inclusions found in natural superdeep diamonds and are expected in lower mantle assemblages²¹.
 48 Combining our new data with *ab-initio* calculations and literature data we directly address the influence of
 49 crystallographic phase transitions on the velocity of capv and apply our results to provide a new understanding of
 50 capv's geophysical signature throughout the lower mantle (Methods).

51 In-line with expectations from previous experiments^{e.g. 18}, *in-situ* diffraction confirms that capv is cubic at high
 52 temperature, and undergoes one (or more) structural distortions upon cooling to room temperature (Figure 2a).
 53 Refinement and indexing of diffraction patterns reveals that endmember CaSiO_3 transforms on cooling from cubic
 54 ($Pm\bar{3}m$) at high temperatures into tetragonal ($I4/mcm$) perovskite between 380 – 420 K at ~ 12 GPa (Figure 2c). This
 55 phase transition is identified by the non-linear splitting upon cooling (observed as broadening) of all diffraction
 56 peaks, except for those with indices *hhh* (i.e. 111 and 222), from the cubic aristotype unit cell ($a \sim 3.5$ Å, Figure 2b
 57 and Extended Data Figure 1e). Additionally, weak superlattice reflections at *d*-spacings of $\sim 2.11, 1.61, 1.07$ and 0.98
 58 Å (Extended Data Figure 2), which uniquely identify the $I4/mcm$ structure, were observed below ~ 420 K. Titanium
 59 incorporation (similarly to aluminium²³) increases the upper stability limit of tetragonal capv considerably, here by
 60 nearly 800 K. We find that $\text{Ca}[\text{Si}_{0.6}\text{Ti}_{0.4}]\text{O}_3$ takes the $Fm\bar{3}m$ space group at high temperature (Extended Data Figure
 61 1,3,4), possessing a double perovskite unit cell, with partial Si:Ti cation ordering that is apparently maintained
 62 throughout cooling. The cubic-tetragonal ($Fm\bar{3}m - I4/m$) transition in $\text{Ca}[\text{Si}_{0.6}\text{Ti}_{0.4}]\text{O}_3$ is observed at ~ 1200 K
 63 (Extended Data Figure 1). Upon further cooling, a subsequent symmetry distortion, thought to be to $P2_1/c$, is
 64 observed at ~ 700 K. These observations provide very strong evidence that capv follows the same structural
 65 transitions on cooling as CaTiO_3 , with the apparent reductions in symmetry from $I4/mcm$ and $Pbnm$ to their $I4/m$
 66 and $P2_1/c$ subgroups being a consequence of cation ordering:



70 Acoustic velocities, determined simultaneously with synchrotron X-ray diffraction using pulse-echo ultrasonic
 71 interferometry, demonstrate that the observed phase transitions of capv are associated with significant elastic
 72 anomalies. CaSiO_3 and $\text{Ca}(\text{Si}_{0.6}\text{Ti}_{0.4})\text{O}_3$ samples undergo v_p and v_s reductions of 4-14 % and 8-20 % respectively due to

73 their cubic-tetragonal transitions (Figure 3). Continued cooling of $\text{Ca}(\text{Si}_{0.6}\text{Ti}_{0.4})\text{O}_3$ into its presumed monoclinic
 74 structure sees the velocities increase near ambient temperature. The acoustic “shear-strengthening” with
 75 temperature that we observe in tetragonal capv is also reported for polycrystalline BaTiO_3 samples²⁵. Such
 76 behaviour is thought to result from a temperature-activated twin-domain wall process that also causes high
 77 acoustic attenuation²⁶. Whilst we cannot rigorously measure acoustic attenuation, we do observe a diminution in
 78 the intensity of reflected acoustic waves when samples are tetragonal. Experiments on endmember CaSiO_3
 79 demonstrate a modest reduction in v_p and v_s across the cubic – tetragonal transition at $T < 450$ K, however the
 80 relatively small decrease observed is likely to continue at sub-ambient temperatures that could not be examined in
 81 this study. We suggest, if cooled further, that CaSiO_3 likely undergoes similar magnitudes of velocity reduction to
 82 those observed for $\text{Ca}(\text{Si}_{0.6}\text{Ti}_{0.4})\text{O}_3$. Absolute acoustic velocities measured for CaSiO_3 are lower than computational
 83 predictions, but v_p and v_s in this study agree extremely well with previous experimental measurements made at
 84 room temperature^{16,17,20}. It is only with increasing temperature that our results diverge from previous experimental
 85 data²⁰. The excellent room temperature agreement leads us to conclude that previous calculations must have
 86 overestimated the velocities, specifically the shear modulus, of capv (as discussed below). We also observe the
 87 temperature dependences of velocities ($\frac{1}{v} \frac{dv}{dT}$) in cubic capv are 1.5 – 3 times larger than experimentally observed for
 88 other mantle silicates^{e.g.} ²⁷. However, the temperature dependence of the elastic moduli in our experiments (dK_s/dT
 89 and $dG/dT \sim -0.027 - -0.03$ GPa K^{-1}) match those observed for cubic $[\text{Ca},\text{Sr}]\text{TiO}_3$ perovskites ($-0.024 - -0.03$ GPa K^{-1})²⁶
 90 and the bulk, but not the shear, modulus in previous experiments on CaSiO_3 ($dK_s/dT \sim -0.036$ and $dG/dT \sim -0.015$
 91 GPa K^{-1})²⁰.

92 Using *ab initio* molecular dynamics, we have calculated the *PT* slope of the $I4/mcm \rightarrow Pm\bar{3}m$ phase transition in
 93 CaSiO_3 perovskite (Methods, Extended Data Figure 5) in order to apply our results to Earth’s deep mantle. The
 94 calculated slope, ~ 15 K GPa^{-1} , is similar to results from previous calculations (~ 10 K GPa^{-1})³ and experiments of the
 95 $I4/mcm \rightarrow Pm\bar{3}m$ transition in SrTiO_3 (~ 18.5 K GPa^{-1})²⁸. However, it is much larger than, but still within uncertainty of,
 96 experimental estimates (≤ 2 K GPa^{-1})^{18,23} for CaSiO_3 . Assuming our *PT* slope is only shifted in temperature by Ti-
 97 incorporation, average MORB capv ($\sim \text{Ca}[\text{Si}_{0.9}\text{Ti}_{0.1}]\text{O}_3$, ignoring other chemical components)¹³ should undergo a cubic
 98 \rightarrow tetragonal transformation at mid-mantle depths. In addition, capv subducted within slab assemblages,
 99 particularly for Ti-rich capv compositions, may in fact retain the tetragonal structure throughout the entire mantle
 100 at average temperatures (Extended Data Figure 5). Pure CaSiO_3 , which is similar to the composition stable in
 101 peridotitic and harzburgitic assemblages, is unlikely to become tetragonal in the ambient mantle, but could undergo
 102 a cubic-tetragonal transition in cold slab assemblages reaching pressures greater than ~ 90 GPa without significant
 103 super-adiabatic heating.

104 To evaluate our experimental results in the context of Earth’s lower mantle we have fitted finite-strain equations of
 105 state (EoS) for cubic and tetragonal CaSiO_3 perovskite, using the thermodynamically self-consistent Mie-Debye-
 106 Grüneisen Birch-Murnaghan formalism²⁹ commonly adopted in mineralogical models⁶. The narrow pressure range of
 107 our experiments means additional constraints from literature data are required for extrapolations where velocities
 108 remain experimentally unconstrained. All available literature data judged to reliably constrain capv volume and/or
 109 acoustic velocities at high *PT* conditions (Supplementary Information Table 1) were collated and converted to a
 110 common pressure scale for joint inversion with new data from this study (see Methods for full fitting procedure).

111 We note that data from recent high-*PT* experiments²⁰ are not included, due to inconsistencies within this dataset
 112 (Methods). Recovered EoS parameters for tetragonal capv at 300 K are $V_0 = 46.10(6) \text{ \AA}^3$ per formula unit, $K_0 = 224(4)$
 113 GPa, $K_0' = 4$ (fixed), $G_0 = 107(6)$ GPa and $G_0' = 1.4(1)$ (Extended Data Figure 6a). The EoS for cubic capv, fitted using
 114 high-temperature data lying above the phase transition calculated by *ab-initio* methods in this study (Figure 1,
 115 Extended Data Figure 6b, Supplementary Information Table 2) has the parameters: $V_0 = 45.57(2) \text{ \AA}^3$, $K_0 = 248(3)$ GPa,
 116 $K_0' = 3.6(1)$, $G_0 = 107(1)$ GPa, $G_0' = 1.66$ (fixed, but manually varied by ± 0.22), $q_0 = 1.1(2)$, $\gamma_0 = 1.67(4)$, $\theta_0 = 771(90)$ K
 117 and $\eta_{s0} = 3.3$ (fixed to $\sim 2\gamma_0$). Incorporation of our newly collected data, compared with only fitting literature data,
 118 improves estimations of G_0 , γ_0 , q_0 and α , due to the high temperature resolution provided by this study, whilst the
 119 dominant constraint on K_0 and K_0' come from the highest-pressure literature data. The narrow pressure range of our
 120 velocity measurements mean they mainly constrain the shear modulus, but not its pressure derivative G_0' . However,
 121 literature values of G_0' from calculations and experiments^{4,5,20} are highly consistent and it can be fixed with some
 122 confidence, although we have also varied it manually to assess its effect on extrapolations. Our approach relies on
 123 high-precision data from four previous diffraction studies on capv at high *PT* conditions and results in a single
 124 equation of state that explains all data without any significant outliers. This provides the best option to date to
 125 investigate capv's velocity at deep mantle conditions and offers self-consistent EoS values without apparent
 126 reduction in predictive capacity throughout the pressures and temperatures relevant to Earth's mantle.

127 Our results imply that cubic capv's compressional and shear velocity profiles are significantly slower than PREM¹⁵
 128 (see Figure 1), whilst its bulk sound velocity is virtually indistinguishable from PREM¹⁵ (Extended Data Figure 7a). We
 129 observe capv's velocities, especially v_s , to be much slower than those predicted from thermodynamic datasets⁶, by
 130 previous high-temperature calculations³⁻⁵, or high *PT* experiments²⁰. In all cases the discrepancy is almost entirely due
 131 to the much lower shear modulus observed in this study. Indeed, it is evident that the shear modulus of capv is one of the
 132 most critical parameters for accurately modelling the velocity of basaltic assemblages throughout the lower mantle. A full
 133 comparison with results from previous studies is provided in the Methods. Whilst titanium-bearing capv has not been
 134 included in finite-strain modelling, our experimental data demonstrates that titanium-incorporation will increase
 135 capv's velocity by $< 1 \text{ km s}^{-1}$ for v_p and $< 0.5 \text{ km s}^{-1}$ for v_s for $\text{Ca}[\text{Si}_{0.6}\text{Ti}_{0.4}]\text{O}_3$. Since MORB-derived capv has an
 136 approximate composition of $\text{Ca}[\text{Si}_{0.9}\text{Ti}_{0.1}]\text{O}_3$ ¹³, the effect of this titanium content on mantle velocities is expected to
 137 be smaller.

138 Understanding the cause of the LLVPs remains one of the most prominent questions currently pursued by the deep
 139 Earth research community³⁰. Identifying whether they are purely thermal anomalies or are thermo-chemical piles of
 140 recycled or primordial material could have profound consequences for our understanding of mantle convection. In
 141 order to address the question of LLVP composition we have incorporated our new cubic capv EoS in thermodynamic
 142 models (Methods, Figure 4), extracting the acoustic velocities of recycled basalt and harzburgite assemblages,
 143 relative to pyrolite, throughout lower mantle conditions (we are assuming pyrolite is representative of average
 144 lower mantle composition). Along a 1500 K mantle adiabat, recycled MORB is predicted to have significantly slower
 145 compressional and shear velocities than pyrolite. This result is in stark contrast with published thermodynamic
 146 datasets, where predicted MORB assemblages are 1-2% faster than the average deep mantle⁶. Thus, despite
 147 geochemical observations implying a long-lived reservoir of recycled crust in the deep Earth³¹ and the high density
 148 of MORB³² favouring its accumulation in the LLVPs^{e.g. 7}, this was previously considered incompatible with observed

149 slow velocities unless temperatures were extremely hot³³. However, our new results now imply LLVPs are well
 150 explained by modest enrichments in recycled oceanic crust, without requiring excess temperature anomalies.
 151 Compared to the bulk mantle composition, which is assumed to be a mixture of approximately 80:20
 152 harzburgite:MORB, the v_s anomalies of -1.5 % and $v_s/v_p > 2$ observed in LLVPs³⁰ can be reproduced by a bimodal
 153 mixture of MORB + harzburgite consisting 64 % MORB at ~ 100 GPa ($v_p = -0.77$ %) or 48 % MORB at ~ 125 GPa ($v_p = -$
 154 0.36 %) if capv is cubic. If the LLVPs are hotter, or if capv is tetragonal near the CMB, the proportion of basalt
 155 required to explain the LLVPs would reduce. Our modelling further implies that the above-average velocities that
 156 surround the LLVPs, lying beneath palaeo-subduction zones that are often considered to be slab-graveyards³⁰, could
 157 potentially represent depleted assemblages. MORB-enriched LLVPs, surrounded by depleted material, also provide
 158 an explanation for the anti- or non-correlation of v_s and v_ϕ in D'' if post-perovskite is stable^{see 30}. Taken at face value,
 159 the predicted properties of CaSiO₃ suggest that pyrolite assemblages may be slightly slower than PREM¹⁵. However,
 160 whilst we are confident that our work robustly demonstrates that subducted MORB assemblages are slow, the
 161 amount of capv in pyrolite is smaller and so further investigations on the effects of titanium and/or aluminium³² in
 162 capv are required to determine whether or not the average velocity of the lower mantle remains compatible with a
 163 pyrolitic bulk composition.

164 The properties of capv also provide an explanation for observed seismic reflectors throughout the mid-mantle². In
 165 very cold slabs following a 1000 K adiabat, subducted basalts (if capv is cubic) are predicted to have very similar
 166 velocities to pyrolitic assemblages on a 1500 K adiabat and so may be seismically invisible. However, if stranded
 167 fragments are thermally equilibrated with surrounding depleted materials, impedance contrasts with magnitudes of
 168 up to $\sim \pm 2.8$ % will be created making them seismically visible as reflectors or as slow regions. Alternatively, if capv
 169 undergoes the cubic-tetragonal phase transition, this may also generate mid-mantle anomalies (Extended Data
 170 Figure 5). Whilst constraining the depth and compositional dependence of this phase transition requires further
 171 studies, it is expected that cold downwelling capv is likely to experience the cubic to tetragonal transformation
 172 somewhere beyond 1000 km depth. Stagnant or delaminated materials in the upper-lower mantle boundary region⁸
 173 may undergo the tetragonal-cubic transition during thermal equilibration, reducing MORB's shear velocity, which
 174 may be the origin of observed mid-mantle reflectors².

175 REFERENCES

- 176 1. Ritsema, J., Deuss, A., van Heijst, H. J. & Woodhouse, J. H. S40RTS: a degree-40 shear-velocity model for the mantle
 177 from new Rayleigh wave dispersion, teleseismic traveltimes and normal-mode splitting function measurements.
 178 *Geophys. J. Int.* **184**, 1223–1236 (2011).
- 179 2. Waszek, L., Schmerr, N. C. & Ballmer, M. D. Global observations of reflectors in the mid-mantle with implications
 180 for mantle structure and dynamics. *Nature Communications* **9**, (2018).
- 181 3. Stixrude, L., Lithgow-Bertelloni, C., Kiefer, B. & Fumagalli, P. Phase stability and shear softening in CaSiO₃ perovskite
 182 at high pressure. *Phys. Rev B* **75**, 024108 (2007).
- 183 4. Kawai, K. & Tsuchiya, T. Small shear modulus of cubic CaSiO₃ perovskite. *GRL* **42**, 2718–2726 (2015).
- 184 5. Li, L. *et al.* Elasticity of CaSiO₃ perovskite at high pressure and high temperature. *PEPI* **155**, 249–259 (2006).
- 185 6. Stixrude, L. & Lithgow-Bertelloni, C. Thermodynamics of mantle minerals - II. Phase equilibria. *Geophys. J. Int.* **184**,
 186 1180–1213 (2011).
- 187 7. Ballmer, M. D., Schmerr, N. C., Nakagawa, T. & Ritsema, J. Compositional mantle layering revealed by slab
 188 stagnation at 1000-km depth. *Science Advances* **1**, e1500815–e1500815 (2015).
- 189 8. Fukao, Y. & Obayashi, M. Subducted slabs stagnant above, penetrating through, and trapped below the 660 km
 190 discontinuity. *JGR* **118**, 5920–5938 (2013).

- 191 9. Stixrude, L. & Lithgow-Bertelloni, C. Geophysics of Chemical Heterogeneity in the Mantle. *Annu. Rev. Earth Planet.*
192 *Sci.* **40**, 569–595 (2012).
- 193 10. Murakami, M., Ohishi, Y., Hirao, N. & Hirose, K. A perovskitic lower mantle inferred from high-pressure, high-
194 temperature sound velocity data. *Nature* **485**, 90–94 (2012).
- 195 11. Cottaar, S., Heister, T., Rose, I. & Unterborn, C. BurnMan: A lower mantle mineral physics toolkit. *Geochem,*
196 *Geophys, Geosy* **15**, 1164–1179 (2014).
- 197 12. Irifune, T. *et al.* Iron partitioning and density changes of pyrolite in Earth's lower mantle. *Science* **327**, 193–195
198 (2009).
- 199 13. Ricolleau, A. *et al.* Phase relations and equation of state of a natural MORB: Implications for the density profile of
200 subducted oceanic crust in the Earth's lower mantle. *JGR* **115**, 2569 (2010).
- 201 14. Liu, L.-G. & Ringwood, A. E. Synthesis of a perovskite-type polymorph of CaSiO₃. *Earth Planet Sci Lett* **28**, 209–211
202 (1975).
- 203 15. Dziewonski, A. M. & Anderson, D. L. Preliminary reference Earth model. *PEPI* **25**, 297–356 (1981).
- 204 16. Sinelnikov, Y. D., Chen, G. & Liebermann, R. C. Elasticity of CaTiO₃-CaSiO₃ perovskites. *PCM* **25**, 515–521 (1998).
- 205 17. Kudo, Y. *et al.* Sound velocity measurements of CaSiO₃ perovskite to 133GPa and implications for lowermost
206 mantle seismic anomalies. *Earth Planet Sci Lett* **349-350**, 1–7 (2012).
- 207 18. Komabayashi, T., Hirose, K., Sata, N., Ohishi, Y. & Dubrovinsky, L. S. Phase transition in CaSiO₃ perovskite. *Earth*
208 *Planet Sci Lett* **260**, 564–569 (2007).
- 209 19. Chen, H. *et al.* Crystal structure of CaSiO₃ perovskite at 28–62 GPa and 300 K under quasi-hydrostatic stress
210 conditions. *Am. Min.* **103**, 462–468 (2018).
- 211 20. Gréaux, S. *et al.* Sound velocity of CaSiO₃ perovskite suggests the presence of basaltic crust in the Earth's lower
212 mantle. *Nature* **565**, 218–221 (2019).
- 213 21. Thomson, A. R., Walter, M. J., Kohn, S. C. & Brooker, R. A. Slab melting as a barrier to deep carbon subduction.
214 *Nature* **529**, 76–79 (2016).
- 215 22. Li, B., Kung, J. & Liebermann, R. C. Modern techniques in measuring elasticity of Earth materials at high pressure
216 and high temperature using ultrasonic interferometry in conjunction with synchrotron X-radiation in multi-anvil
217 apparatus. *PEPI* **143**, 559–574 (2004).
- 218 23. Kurashina, T., Hirose, K., Ono, S., Sata, N. & Ohishi, Y. Phase transition in Al-bearing CaSiO₃ perovskite: implications
219 for seismic discontinuities in the lower mantle. *PEPI* **145**, 67–74 (2004).
- 220 24. Yashima, M. & Ali, R. Structural phase transition and octahedral tilting in the calcium titanate perovskite CaTiO₃.
221 *Solid State Ionics* **180**, 120–126 (2009).
- 222 25. Salje, E. K. H. *et al.* Elastic excitations in BaTiO₃ single crystals and ceramics: Mobile domain boundaries and polar
223 nanoregions observed by resonant ultrasonic spectroscopy. *Phys. Rev. B* **87**, 014106 (2013).
- 224 26. Perks, N. J., Zhang, Z., Harrison, R. J. & Carpenter, M. A. Strain relaxation mechanisms of elastic softening and twin
225 wall freezing associated with structural phase transitions in (Ca,Sr)TiO₃ perovskites. *J. Phys.: Condens. Matter* **26**,
226 505402 (2014).
- 227 27. Liu, Z. *et al.* Elastic wave velocity of polycrystalline Mj₈₀Py₂₀ garnet to 21 GPa and 2,000 K. *PCM* **42**, 213–222 (2015).
- 228 28. Guennou, M., Bouvier, P., Kreisel, J. & Machon, D. Pressure-temperature phase diagram of SrTiO₃ up to 53 GPa.
229 *Phys. Rev B* **81**, (2010).
- 230 29. Stixrude, L. & Lithgow-Bertelloni, C. Thermodynamics of mantle minerals - I. Physical properties. *Geophys. J. Int.*
231 **162**, 610–632 (2005).
- 232 30. Garnero, E. J., McNamara, A. K. & Shim, S.-H. Continent-sized anomalous zones with low seismic velocity at the
233 base of Earth's mantle. *Nature Geosci* **9**, 481–489 (2016).
- 234 31. Hofmann, A. W. Mantle geochemistry: the message from oceanic volcanism. *Nature* **385**, 219–229 (1997).
- 235 32. Hirose, K., Fei, Y., Ma, Y. & Mao, H.-K. The fate of subducted basaltic crust in the Earth's lower mantle. *Nature* **397**,
236 53–56 (1999).
- 237 33. Deschamps, F., Cobden, L. & Tackley, P. J. The primitive nature of large low shear-wave velocity provinces. *Earth*
238 *Planet Sci Lett* **349-350**, 198–208 (2012).

239 ACKNOWLEDGEMENTS

240 We acknowledge the support of NERC grants NE/PO17657/1 and NE/M00046X/1, and ESRF beamtime proposals ES-
241 464 and ES-636. We thank G. Manthilake and D. Freitas for their assistance and for lending us ultrasonic equipment
242 from Laboratoire Magmas et Volcans for use during the initial experiments of this study. Use of Pixirad-8 detector
243 was supported by the French Government via the "Investissements d'Avenir" program, under the reference ANR-10-
244 AIRT-05.

245 AUTHOR CONTRIBUTIONS

246 A.R.T. designed, performed and analysed the experiments, gathered data from the literature and wrote the
 247 manuscript. W.A.C. designed and developed the experimental procedure at ID06 of the ESRF. I.G.W. assisted with
 248 interpretation and refinement of diffraction data. J.P.B., D.P.D, W.A.C and N.C.S. helped perform experiments over
 249 two sessions at the ESRF. J.M. performed the computational simulations. S.A.H. assisted with data analysis. All
 250 authors contributed to the scientific discussion and preparation of the manuscript.

251 AUTHOR INFORMATION

252 The authors declare no competing financial interest. Correspondence and requests for materials should be
 253 addressed to A.R.T (a.r.thomson@ucl.ac.uk).

254 DATA AVAILABILITY STATEMENT

255 Raw data were collected at the European Synchrotron Radiation Facility in Grenoble and are available from
 256 <http://doi.org/10.5285/6db95d87-365f-4018-abec-00e96e8fcf8d>. Derived data from this study, which includes
 257 source data from figure 2 & 3 and extended data figures 1 & 5, are provided in the supplementary information
 258 tables.

259 FIGURE CAPTIONS

260 **Figure 1: Compressional and shear wave velocities of cubic CaSiO₃ perovskite from this and previous studies** (a)
 261 compressional wave velocity and (b) shear wave velocity of CaSiO₃ perovskite predicted in this, and previous,
 262 studies throughout the mantle. Individual experimental measurements are shown with symbols, coloured by
 263 temperature (white symbols are data collected at 300 K). All velocity curves are extracted along a 1500 K mantle
 264 adiabat. Thick coloured curve (and 95% confidence interval in grey) represents velocity of cubic capv based on
 265 finite-strain modelling (this study). Bold dashed line is the PREM velocity profile.

266 **Figure 2: X-ray diffraction patterns demonstrating the cubic-tetragonal phase transition in CaSiO₃ perovskite.** (a)
 267 Rietveld refined X-ray diffraction patterns collected at ~ 12 GPa and 1273 K (red, cubic) or 300 K (blue, tetragonal),
 268 with cubic CaSiO₃ peaks labelled by *hkl* and tick marks for other cell components, (b) normalised full-width-at-half-
 269 maximum (fwhm) of selected diffraction peaks of CaSiO₃ perovskite as a function of temperature, (c) refined lattice
 270 parameters of CaSiO₃ perovskite sample as a function of experimental temperature with 2σ uncertainties.

271 **Figure 3: Acoustic velocities of capv samples at high *PT* conditions.** (a) Compressional, v_p , and (b) shear, v_s , velocities,
 272 with derived (c) shear, G , and (d) bulk, K_s , moduli of capv samples measured as a function of temperature at
 273 constant press load (~ 12 GPa), for Ca(Si_{0.6}Ti_{0.4})O₃ (blue circles) and CaSiO₃ samples (orange and green circles).
 274 Uncertainties are all 2σ. Small blue circles are data with a low signal:noise ratio, due to low amplitude of the buffer
 275 rod reflection, and have larger uncertainties. Experimental velocity measurements from previous studies are plotted
 276 as triangles (~ 12 GPa) and squares (orange 12±1 GPa and purple at 15±1 GPa). Dashed vertical lines indicate the
 277 temperatures of observed phase transitions for CaSiO₃ (orange) and Ca(Si_{0.6}Ti_{0.4})O₃ (blue). The blue temperature
 278 interval represents the extent of the 1st order *I4/m* to *P2₁/c* transition in Ca(Si_{0.6}Ti_{0.4})O₃.

279 Figure 4: **Modelled velocity profiles of lower mantle phase assemblages incorporating capv based on this study.**
280 Models of (a) MORB, (b) harzburgite phase assemblages relative to pyrolite throughout the lower mantle. Red
281 curves are calculated velocity profiles along a self-consistent 1500 K adiabat, blue curves are calculated along a
282 1000 K adiabat. Solid curves are compressional velocities, dashed are shear velocities, and dotted curves are bulk
283 sound velocity profiles. The upper edge of each curve is the velocity when capv is cubic, whereas the lower bound is
284 indicative of the velocity expected if capv forms a tetragonal structure.

285 METHODS

286 STARTING MATERIALS

287 Starting materials of CaSiO_3 and $\text{Ca}[\text{Si}_{0.6}\text{Ti}_{0.4}]\text{O}_3$ compositions were initially prepared by grinding appropriate
288 quantities of high purity CaCO_3 , SiO_2 and TiO_2 together in an agate mortar, prior to decarbonation and sintering into
289 crystalline wollastonite, in the case of CaSiO_3 , or fusing to a glass, for $\text{Ca}[\text{Si}_{0.6}\text{Ti}_{0.4}]\text{O}_3$. All materials were analysed
290 with SEM EDS to check composition, and the CaSiO_3 was confirmed as pure wollastonite using X-ray powder
291 diffraction ($\lambda = 1.7904 \text{ \AA}$). Ultrasonic experiments require fully-dense cylindrical samples with parallel polished
292 faces and an aspect ratio of the length/diameter < 2 . Thus, the $\text{Ca}[\text{Si}_{0.6}\text{Ti}_{0.4}]\text{O}_3$ glass was hot-pressed into capv at \sim
293 14 GPa and 1400 °C using a 10/5 multi anvil assembly, and the recovered products manipulated into suitable forms
294 for subsequent acoustic experiments. Since CaSiO_3 perovskite is unrecoverable, undergoing a decomposition to
295 amorphous “glass” with significant fracturing at room temperature, it is not possible to prepare a similar sample of
296 the endmember perovskite composition. Instead samples of walstromite were prepared, which is the highest-
297 pressure recoverable polymorph of CaSiO_3 , by sintering at ~ 7 GPa and 1300 °C using a 14/8 multi-anvil assembly.

298 DIFFRACTION AND ULTRASONIC EXPERIMENTAL METHODS

299 X-ray diffraction and pulse-echo ultrasonic experiments were performed on beamline ID06-LVP of the ESRF
300 synchrotron, where modified 10/5 multi anvil assemblies were employed to allow simultaneous measurement of
301 sample diffraction, length and acoustic velocity. Samples were placed adjacent to a polished polycrystalline alumina
302 buffer rod on one side that reached the cube to which the ultrasonic transducer was attached, and an MgO + NaCl
303 mixture serving as soft backing and (for the NaCl) as a pressure marker on the other. Thin Au foils were placed at
304 each end of the sample to allow sample length to be observed with radiographic imaging, and also between the
305 cube and buffer rod to assist with acoustic coupling. This acoustic column was encapsulated in a crushable MgO
306 sleeve, and subsequent Re or TiB_2 +BN furnace, which was contained within ZrO_2 insulation and a Cr:MgO octahedral
307 pressure medium. A W-Re thermocouple was used, inserted from the opposite end of the cell assembly in an MgO
308 sleeve to monitor temperature adjacent to the sample throughout experiments (Extended Data Figure 8c).

309 Along the path of the x-ray beam, the normal ceramic materials were replaced by high transparency amorphous
310 SiBCN(O) windows. Monochromatic synchrotron x-rays ($\lambda = 0.22542 \text{ \AA}$ or 0.2296 \AA) were used to collect diffraction
311 patterns from the sample and pressure markers throughout experiments using two different detectors available at
312 ID06. In all experiments the standard Detection Technology X-scan 1D detector³⁴, which has a fixed 10 Hz
313 integration rate was used to record diffraction patterns every 3.2 (continuous, with 32X rebin)-32 seconds
314 (punctual, on increasing and decreasing pressure). Throughout one experiment on CaSiO_3 an additional Pixirad-8
315 detector was employed to assist with the identification of weak superlattice reflections from the sample. X-ray

316 sample-detector geometry was calibrated using Si and/or LaB₆ NIST standards, and the collected diffraction patterns
317 were suitably reduced and analysed using the Fit2d³⁵ software. Rietveld refinement of selected diffraction patterns
318 was performed using the GSAS software package³⁶ (Supplementary Information Table 3 & 4). Experimental unit-cell
319 volumes were also determined, and used for *PVT* EoS determination, by fitting the position and width of individual
320 diffraction lines from the capv samples and pressure markers. In this case capv volumes are determined using the
321 average volume calculated from the 200, 310, 321 and 222 diffraction peaks of the sample, whilst the volume of
322 NaCl and Au were determined using their 220 and 310 peaks respectively (Supplementary Information Table 5).

323 Samples were compressed to target load and initially heated to $T > 1000$ K to remove stress in the sample that
324 might affect acoustic measurements. In the experiments on CaSiO₃, the starting material of walstromite was
325 converted into capv by annealing at constant load (initial pressure ~ 14 GPa) and 1200-1500 K for a period of 2-4
326 hours, until all signs of walstromite diffraction peaks were lost. Pressure throughout the experiments was
327 determined from the unit-cell volumes of NaCl-B1 and/or Au using cross-calibrated high-temperature equations of
328 state³⁷, whilst sample length was measured using the standard imaging system installed on ID06-LVP. Sample
329 lengths determined with x-ray imaging were checked against those measured before and after (in the case of
330 Ca[Si_{0.6}Ti_{0.4}]O₃) experiments with a digital gauge (1 μm accuracy). Uncertainties in sample lengths are estimated
331 from images as ± 5 pixels, corresponding to $\pm 5.4\mu\text{m}$ ($< 2\%$ overall sample length), and it is this uncertainty that
332 produces the reported uncertainties in velocities (Supplementary Information Table 6 and Figure 3). Alongside
333 ultrasonic measurements accompanied by diffraction and imaging, the crystallographic evolution of the samples
334 was specifically investigated using continuous diffraction collected during constant rate cooling ramps (25 – 50
335 Kmin^{-1}) for CaSiO₃ and Ca[Si_{0.6}Ti_{0.4}]O₃ samples without collecting ultrasonic data.

336 Acoustic signals, always collected after sample annealing at high T , were transmitted into and received from the
337 sample assembly using a 10° Y-cut dual mode LiNbO₃ piezoelectric transducer that was fixed to the corner of the
338 “acoustic cube” opposite to the sample using Epo-tek 353ND epoxy. A signal generator (Tektronix AFG3101C or
339 Keysight 33622A) was used to create acoustic pulses composed of three consecutive periods of sine waves with 30-
340 60 MHz frequency and $\pm 2.5 - 5$ V amplitude, which were passed to the transducer and oscilloscope. The resonant
341 frequency of v_p and v_s from the transducer crystal were ~ 50 and 30 MHz respectively. Received echoes were
342 measured using the same oscilloscope (Tektronix DPO5140 or Keysight DSOS104A) to record the delay between
343 arrival times of compressional and shear wave signals at a rate of $2.5 - 5 \times 10^9$ samples/s. In later experiments a
344 directional bridge (Keysight 86205A), preamplifier (LA020-OS) on the return signal and external trigger (trigger rate
345 2 kHz) were variously used, as the system was continuously developed throughout this study. Collection times of
346 individual acoustic spectra ranged from 5 - 300 s, with the various systems employed throughout this study. Two-
347 way travel times of ultrasonic arrivals were converted into sample velocities using the “pulse-echo overlap method”
348 (for reflections from the near and far ends of the sample), which was implemented by maximising absolute values of
349 signal cross-correlation and sample lengths measured with x-ray imaging. Predicted reflection coefficients for both
350 interfaces (based on $R = (Z_2 - Z_1)/(Z_1 + Z_2)$, with $Z_i = \rho_i v_i$) are both negative (~ -0.025 and -0.25 for Al₂O₃ – capv and capv
351 – NaCl+MgO respectively) at the *PT* conditions of the experiments, suggesting that no phase shift is expected in the
352 acoustic signals. The lack of observed phase shifts and measured pulse/echo amplitude ratios were found to be
353 consistent with these expectations, which provides assurance that the phase of acoustic arrivals has been correctly

354 identified. Measured velocities are reported in Supplementary Information Table 6. It should be noted that two
 355 independent experiments were performed to measure the velocity of CaSiO_3 samples (which agree within
 356 uncertainty for v_p) during separate visits to the ESRF, one employing a Re and the other a TiB_2 :BN furnace. In the
 357 second of these experiments on CaSiO_3 , the shear wave signal from the sample was not observable above noise
 358 levels and thus the shear-wave velocity was not determined. Additionally, the ultrasonic data reported for
 359 $\text{Ca}[\text{Si}_{0.6}\text{Ti}_{0.4}]\text{O}_3$ above 975 K were collected on heating after annealing, whilst data below 975 K was subsequently
 360 collected upon cooling the sample. This results in a small pressure difference between the two sets of
 361 measurements and explains the discontinuity in Figure 3.

362 STRUCTURE DETERMINATION

363 Refined diffraction data from experiments on CaSiO_3 are consistent with a cubic crystal structure for capv at high
 364 temperatures. All observed diffraction peaks have approximately constant widths at half maximum intensity, in line
 365 with expectations from the diffractometer geometry, and all observed diffraction peaks could be attributed to
 366 diffraction from the sample (in space group $Pm\bar{3}m$) or other cell components (MgO , Au, NaCl, TiB_2 , Al_2O_3). Upon
 367 cooling, the diffraction peaks from the sample undergo significant non-linear hkl -dependent broadening below \sim
 368 420 K (Figure 2 and Extended Data Figure 1e). Similarly to previous studies^{18,23} we interpret this observation as the
 369 result of a cubic-tetragonal transition in CaSiO_3 . Close inspection of diffraction data from the Pixirad-8 detector,
 370 which was employed during one experiment, reveals that weak superlattice peaks from CaSiO_3 (otherwise
 371 unexplained by other cell components) appear in data collected at 373 and 300 K (Extended Data Figure 2). The
 372 strongest of these is observed at $2\theta \sim 6.1^\circ$ (indexed as $3/2 \ 1/2 \ 1/2$ on the cubic sub-lattice) but additional peaks can
 373 also be observed at 8.05° ($3/2 \ 3/2 \ 1/2$), 12.1° ($5/2 \ 3/2 \ 3/2$) and 13.2° ($5/2 \ 5/2 \ 1/2$) (d -spacings of $\sim 2.11, 1.61, 1.07$
 374 and 0.98 \AA). Assuming that CaSiO_3 's initial distortion upon cooling is to a tetragonal phase, there are three likely
 375 candidate structures, with space groups $I4/mcm$, $P4/mbm$ and $I4/mmm$. The predicted superlattice peak positions
 376 for the structure with $I4/mcm$ symmetry exactly match the observed superlattice peak positions, explaining all four
 377 observed peaks, whilst CaSiO_3 structures with space groups $P4/mbm$ or $I4/mmm$ cannot account for the
 378 observations (Extended Data Figure 2) as these should both produce many additional superlattice peaks (e.g. those
 379 indexed as $1/2 \ 0 \ 3/2$, $3/2 \ 1/2 \ 1/2$, $1/2 \ 0 \ 5/2$, $5/2 \ 1/2$ etc. on the basis of the cubic sub-cell) that are not observed. Given
 380 that there are no additional unexplained diffraction peaks, the knowledge that the most obvious superlattice peak
 381 at $\sim 6.1^\circ$ 2θ should indeed be the strongest in $I4/mcm$ and that the same transition ($Pm\bar{3}m$ to $I4/mcm$) occurs in
 382 CaTiO_3 ²⁴, we see no reason to doubt the structure of CaSiO_3 at room temperature and $\sim 12 \text{ GPa}$ is tetragonal with
 383 space group $I4/mcm$.

384 The observed behaviour of $\text{Ca}[\text{Si}_{0.6}\text{Ti}_{0.4}]\text{O}_3$ is similar to CaSiO_3 , but the intensities of the superlattice peaks are much
 385 greater and the material is recoverable to ambient conditions. Diffraction patterns collected from the starting
 386 material $\text{Ca}[\text{Si}_{0.6}\text{Ti}_{0.4}]\text{O}_3$ (measured alongside LaB_6 as a calibrant at 300 K, Extended Data Figure 3a) allows
 387 identification of superlattice peaks with odd and even Miller indices, which requires positive and negative
 388 octahedral tilts³⁸. Thus, the highest possible symmetry of $\text{Ca}[\text{Si}_{0.6}\text{Ti}_{0.4}]\text{O}_3$ at ambient conditions is orthorhombic.
 389 Refining the diffraction data in three likely spacegroups ($Pbnm$, $Cmcm$ and $P4_2/nmc$) demonstrates that both $Pbnm$
 390 and $Cmcm$ can explain the patterns equally well, and so it is concluded ambient $\text{Ca}[\text{Si}_{0.6}\text{Ti}_{0.4}]\text{O}_3$ is orthorhombic
 391 (actually monoclinic when B-cation ordered, see below). We choose to assume the space group is $Pbnm$, as this is

392 the known structure of CaTiO_3 ²⁴. Since no phase transition is observed during decompression, the room-
393 temperature structure at high pressure is also assumed to be $Pbnm$, or its B-cation ordered equivalent ($P2_1/c$). At
394 high- PT conditions $\text{Ca}[\text{Si}_{0.6}\text{Ti}_{0.4}]\text{O}_3$ is observed to undergo two structural phase transitions (Extended Data Figure 4).
395 At the highest temperatures, the diffraction pattern is well explained if the sample takes a cubic $Fm\bar{3}m$ structure.
396 With respect to the cubic form of CaSiO_3 , this has a double unit-cell edge length and partial B-cation ordering
397 (assumed to follow a 1:1 B-site scheme³⁹) of Si and Ti, a common ordering scheme in perovskites. On cooling, the
398 $\text{Ca}[\text{Si}_{0.6}\text{Ti}_{0.4}]\text{O}_3$ first distorts to a tetragonal structure marked by the appearance of the same set of superlattice
399 peaks that were observed for CaSiO_3 . Since the cubic Ti-bearing capv is B-cation ordered, it is assumed the
400 tetragonal phase maintains this B-cation cation ordering, making the space group of the tetragonal phase $I4/m$.
401 Continued cooling sees distortion into the room temperature phase, which is assigned to be monoclinic $P2_1/c$ (the
402 B-cation ordered variant of $Pbnm$). Between the tetragonal and monoclinic structures there is a temperature
403 interval where the diffraction pattern cannot be indexed using a single structure model, and it is observed that this
404 temperature interval corresponds to very low acoustic velocities. This may be indicative of a first-order phase
405 transition, which further implies a preference for $Pbnm$ or $P2_1/c$ over $Cmcm$ or $C2/c$, based on the analysis of
406 Glazer³⁸. Alternative explanations for this behaviour are a temperature interval of phase coexistence, an additional
407 perovskite structure or some other unexplained phenomena. Similar observations have been made for CaTiO_3 ⁴⁰,
408 where there is a small temperature interval between the $I4/mcm$ and $Pbnm$ structures where the behaviour is
409 attributed to an interval of phase coexistence caused by the kinetic energy barrier of the first-order phase
410 transition. A more detailed discussion of the crystallographic behaviour of capv samples lies beyond the scope of
411 the current study.

412 AB-INITIO CALCULATIONS AND THE SLOPE OF THE CAPV TETRAGONAL-CUBIC TRANSITION

413 *Ab-initio* calculations were performed to constrain the conditions of the tetragonal – cubic transition of capv
414 throughout the Earth's mantle. All simulations were carried out with the density-functional-theory (DFT) code
415 VASP⁴¹ using the projector-augmented-wave (PAW) method⁴² and the PBE formulation of generalised-gradient-
416 approximation (GGA)⁴³. Molecular dynamics (MD) calculations used the Nosé thermostat and were run at the
417 gamma point with a cut-off of 600 eV and relaxed to within 10^{-5} eV and all forces to below 0.03 eV/Å. All
418 computational runs were at least 20 ps in duration, although all measured properties were observed to be fully
419 converged by 12 ps. Phonon calculations for calculating the force-constant matrix used an energy cut off of 850 eV,
420 $4 \times 4 \times 4$ K points and were relaxed to 10^{-8} eV with forces below 0.01 eV/Å. The finite difference method was used and
421 processing was done with the phonopy code⁴⁴. Ca atom semicore 3s and 3p states were treated as valence states.
422 All static and molecular dynamics runs were spin-polarised and CaSiO_3 was always simulated with an 80 atom
423 simulation box, based on a $2 \times 2 \times 4$ assemblage of the perovskite cubic aristotype cell containing 5 atoms. For cubic
424 perovskite calculations the sub-cells from which the simulation box was constructed were fixed to have a geometry
425 of $a=b=c$, whereas for tetragonal CaSiO_3 the simulation geometry for was fixed such that $a=b \neq c$. Details of
426 simulation cell volumes are provided in Supplementary Information Table 7. In each case the final stress on the
427 crystal was correct to within 0.04 GPa for static calculations and to within 0.1 GPa (on average) for MD calculations.
428 After the geometries were imposed at each PT condition the atoms were allowed to relax, within constraints
429 maintaining cubic or tetragonal structure, prior to simulations used to obtain free energies.

430 Free energy differences were calculated at 25, 75 and 125 GPa and at 0, 1000, 2000 and 3000 K. To calculate the
 431 free energy of each state we used an approximation of the thermodynamic integration represented by eq. 1:

$$432 \quad F - F_0 \cong \langle U - U_0 \rangle_0 + \frac{1}{2k_bT} \langle [U - U_0 - \langle U - U_0 \rangle_0]^2 \rangle_0 \quad (\text{eq. 1})$$

433 Where subscript 0 represents the reference state and other terms the state of interest. For a reference state we
 434 used a harmonic oscillator with free energy defined by eq. 2:

$$435 \quad U_0 = U + \sum_i \frac{p_i^2}{2m_i} + \frac{1}{2} \sum_{ij} \mathbf{u}_i \Phi_{ij} \mathbf{u}_j \quad (\text{eq. 2})$$

436 where \mathbf{u}_x is a displacement vector and Φ_{ij} is the force constant matrix. As cubic CaSiO_3 is unstable at low
 437 temperatures it has negative frequencies in its phonon spectrum and the free energy cannot be calculated directly
 438 from its force constant matrix. Thus, we applied a small correction to eliminate these imaginary frequencies and
 439 allow free energy calculations. The correction matrix (Φ_{ij}^c) is formed by multiplying the onsite terms in the force
 440 constant matrix by kI (where I is the identity matrix and k is the smallest constant that eliminates all imaginary
 441 frequencies). The correction procedure then subtracts the correction matrix from the true force constant matrix
 442 ($\Phi_{ij} - \Phi_{ij}^c$) to produce a modified force constant matrix Φ_{ij}^* which is used in eq. 2. Whilst this procedure cannot
 443 predict the correct absolute free energies, it should accurately calculate the free energy difference relative to a
 444 reference state that has had the same correction procedure applied. This procedure is repeated for both cubic and
 445 tetragonal CaSiO_3 structures at each PT condition, and finally the free energy difference between these states is
 446 determined using eq. 3:

$$447 \quad \Delta G_{\text{cub-tet}} = \Delta G_{\text{final-ref}}^{\text{cub}} + G_{\text{ref}}^{\text{cub}} - (\Delta G_{\text{final-ref}}^{\text{tet}} + G_{\text{ref}}^{\text{tet}}) \quad (\text{eq. 3})$$

448 The final calculated free energy differences between cubic and tetragonal states are reported in Supplementary
 449 Information Table 7. All free energy differences are subject to uncertainties, which are assumed to be 1 meV/fu at
 450 0K, and calculated to be < 10 meV/fu at high temperatures, from the statistical uncertainty in the simulation
 451 energies. These uncertainties were incorporated in the weighted least-squares regression used to determine the
 452 conditions and uncertainty of the tetragonal-cubic transformation at each pressure (25, 75 and 125 GPa) as plotted
 453 in Extended Data Figure 5.

454 CALCIUM PEROVSKITE EQUATION OF STATE

455 PVT-velocity data from experiments in this, and literature, studies were combined to allow fitting of an equation of
 456 state (EoS) for both tetragonal and cubic CaSiO_3 perovskite. The pressures of all reported literature data were
 457 converted to a single pressure-scale, which was used for pressure measurement in this study³⁷. This ensures
 458 consistency of the pressure-scale used throughout the dataset. The fitted EoS for tetragonal capv uses only room
 459 temperature data and all literature data collected on samples compressed in diamond anvil cells without use of a
 460 pressure-transmitting-medium were discarded (small symbols in Extended Data Figure 6a). The remaining PV
 461 data^{19,45}, including 1/20th of the data collected during room temperature decompression in this study prior to

462 amorphisation, were fitted to a second-order Birch Murnaghan EoS for V_0 and K_{T0} using the BurnMan software
 463 package¹¹ (Supplementary Information Table 2). Only 1/20th of the current data were used to ensure the final fitted
 464 model was not overly biased to the data collected in this study. Subsequently, room temperature velocity
 465 measurements from this study were combined with literature data^{17,20} to fit the shear modulus (G_0) and its pressure
 466 derivative (G_0') within the SLB2005²⁹ formalism, as provided in BurnMan. As the equation of state is only calibrated
 467 at room temperature, estimates of velocity reductions for tetragonal capv in Figure 4 are qualitatively based on the
 468 magnitude of reductions observed in measurements from Ca[Si_{0.6}Ti_{0.4}]O₃, taken ~ 100 K below the phase transition,
 469 in this study, and are not calculated by using the tetragonal capv EoS.

470 The EoS for cubic capv (Supplementary Information Table 2) also fits data from this study and the literature⁴⁵⁻⁴⁸ using
 471 the SLB2005²⁹ Mie-Grüneisen-Debye Birch-Murnaghan formalism implemented in BurnMan¹¹. Only data falling
 472 above the calculated *PT* curve of the tetragonal-cubic phase transition (Extended Data Figure 5) were used to
 473 ensure that no data from tetragonal-structured capv were included (Extended Data Figure 6b). *PVT* data were first
 474 used to fit V_0 , K_0 , K_0' and γ_0 . Subsequently, the complete *PVT*-velocity dataset was re-fitted for G_0 , γ_0 , q_0 and θ (V_0 ,
 475 K_{T0} , K_0' were unchanged) assuming $G_0' = 1.66$. G_0' was fixed to literature values^{4,5,20} due to the small pressure range
 476 of velocity measurements in this study, a value consistent with literature scaling rules²⁹. η_{s0} was fixed at 3.3, based
 477 on the scaling rules ($\eta_{s0}/\gamma_0 \sim 2$) from Stixrude²⁹. Alternatively, η_{s0} can also be a fitted parameter (Supplementary
 478 Information Table 2). However, since this second fit (with variable η_{s0}) results in slightly lower extrapolated
 479 velocities without significantly altering subsequent interpretation, fixing η_{s0} was viewed as a more conservative way
 480 to evaluate the influence of capv. It is noted that the uncertainty bounds plotted in Figure 1 account for variation of
 481 G_0' from 1.44 – 1.88 and capv remains slower than PREM and *ab initio* estimates throughout this entire range. We
 482 recognise that, without using literature data, extrapolation throughout the mantle pressure range would be
 483 completely unrealistic – and are beholden to accepting the reliability of literature data; however we note that four
 484 previous studies on capv at high *PT* conditions, after conversion to a common pressure scale, can be combined and
 485 fitted to a single equation of state without any significant outliers. Readers are referred to Stixrude²⁹ for details of
 486 the SLB2005 formalism.

487 THERMODYNAMIC MODELLING

488 The acoustic properties of MORB, peridotitic and harzburgitic assemblages have been calculated using the MMA-
 489 EoS software package⁴⁹. Simplified bulk compositions for MORB (NCFMAS) and pyrolite/harzburgite (CFMAS) from
 490 the software's library were employed as typical of these assemblages throughout the lower mantle. Equilibrium
 491 phase assemblages were calculated across a 0.5 GPa by 25 K grid throughout the mantle for each system, and the
 492 elastic properties of each assemblage extracted along self-consistent adiabatic temperature profiles beginning at
 493 1000 K (representing slabs) and 1500 K (average mantle), which are plotted relative to one-another in Figure 4. The
 494 latter temperature profile is very similar to the geotherm of Brown and Shankland⁵⁰. Thermoelastic data from
 495 Stixrude⁶ was used for all phases except for the MgSiO₃ bridgmanite endmember (which used updated properties
 496 from Zhang⁵¹) and calcium perovskite which is defined in this study. We note that this database provides a
 497 somewhat simplified view of lower mantle materials, as it does not include the effects of iron spin-transitions in
 498 ferropericlase or bridgmanite^{e.g. 52,53} or the ferroelastic phase transitions of stishovite^{e.g. 54}. We also highlight that the

499 modelling in this study inherently assumes that the database from Stixrude et al.⁶ accurately describes the elastic
500 properties of all other lower mantle phases.

501 COMPARISON WITH PREVIOUS STUDIES

502 As noted in the main text, the acoustic velocities of CaSiO₃ observed in this study are observed to be significantly
503 slower than predicted in computational studies³⁻⁵ and mineralogical databases⁶. Additionally, they are also observed
504 to be slower than those found in previous high *PT* experiments²⁰. Whilst we cannot fully explain the reasons for all
505 disagreements, we discuss some observations that may partially explain the mismatches. Database elastic
506 properties⁶ predict the fastest capv velocities plotted in Figure 1, and it is these that the Earth Science community
507 currently uses when interpreting seismic observations. Results from the two ab initio molecular dynamics (AIMD)
508 computational studies^{4,5} and experiments²⁰ all predict that capv should be equal to (v_p) or slower (v_s) than PREM. If
509 any of these results were adopted in mineralogical databases, slow velocity anomalies in the lower mantle could be
510 interpreted as they are in this study, an indicator of MORB enrichment, although not to the extent implied here. We
511 note that the other pseudo-high-temperature calculations³ do not provide enough information in the paper to
512 calculate acoustic properties at elevated temperatures, since the temperature effect on density is unquantified in
513 the original publication.

514 Comparing our work in detail, first with previous experimental results, it is observed that the room-temperature velocities
515 measured in this study are in excellent agreement with those of Gréaux et al.²⁰, Kudo et al.¹⁷ and extrapolated estimates
516 from Sinelnikov et al.¹⁶. Room-temperature velocities measured by Li et al.²² are somewhat faster, but given the lack of
517 details provided in that paper, which is a technical review, they are not considered further. It is observed that our reported
518 velocities disagree from previous experimental data only at high temperature²⁰, appearing to diverge as the reported
519 temperature increases. Given the similarities in methodology, it is most likely that temperature uncertainties are
520 responsible for the differences. Based on published details, we believe Gréaux et al.²⁰ employed samples of 0.93-1.3 mm
521 length (Figure 2 and Extended Data Figure 3 of Gréaux et al.²⁰) and 2mm diameter, with the thermocouple inserted radially
522 (through the furnace) adjacent to the far end of the pressure marker that in their experiments is initially ~ 1 mm in length.
523 This arrangement is substantially larger than the samples used in this study, which were 0.4-0.6 mm in length and 1.5 mm
524 diameter, with the thermocouple inserted axially to the end of the pressure marker that had a maximum length of 0.5 mm.
525 Thus, the maximum distance between the thermocouple and far end of the sample in our study is 1.1 mm, likely 0.75 mm
526 at high pressure, approximately half of the equivalent distance in Gréaux et al.²⁰ (likely ≥ 1.5 mm at pressure). Additionally,
527 by inserting the thermocouple axially in the cell at high-pressure, whereas it is unclear whether or not this would be the
528 case with a radial thermocouple, which could also have been affected by contacting the metal furnace. Given that, at 12-22
529 GPa, the sample column is likely to be 4-5 mm in length, the differences in geometry might have a very large influence on
530 the temperature conditions experienced by samples. Thermal modelling using finite element code⁵⁵ suggests that the
531 thermal gradient across samples at a measured temperature of 1200 °C in our setup should be < 50-60 °C, with the
532 measured temperature likely to be lower than peak conditions. In contrast, assuming the thermocouple is centred (as
533 drawn by Gréaux et al.²⁰) and measuring 1200 °C, the range of temperatures experienced by a sample of 1 mm length x 2
534 mm diameter could very conceivably be 250 - 300 °C lower than that measured by the thermocouple. This implies that the
535 apparent effect of temperature on velocities should be smaller using the geometry of Gréaux et al.²⁰, since portions of
536 samples would be colder than believed. This is consistent with the observed differences in velocities between Gréaux et

537 al.²⁰ and the present study, where the offset in reported velocities increases at higher temperatures. Additional evidence
 538 that the high-temperature velocities reported by Gréaux et al.²⁰ might be less reliable is demonstrated by comparing the
 539 independent estimates of bulk sound velocity expected for capv from pressure-temperature-volume systematics and
 540 acoustic measurements ($V_\phi = \sqrt{V_P^2 - \frac{4}{3}V_S^2} = \sqrt{K_S/\rho}$, where K_S is a function of K_{OT} , K' , γ and α). We observe that the bulk
 541 sound velocity extracted from ultrasonic measurements in Gréaux et al.²⁰ are inconsistent with velocity extracted via a *PVT*
 542 EoS using their diffraction data (Extended Data Figure 9). Ultrasonic V_ϕ values from Gréaux et al.²⁰ are offset to slower
 543 values and have a much larger reduction at high temperature than those predicted *via* an EoS fitted using density
 544 from their or compiled literature data⁴⁵⁻⁴⁸. In contrast, bulk sound velocities from data in this study are consistent with
 545 literature *PVT* EoS fitting. This inconsistency suggests velocities reported in Gréaux et al.²⁰ might be affected by large
 546 temperature gradients.

547 Considering calculated properties of capv, we observe that the database values³ best reproduce the adiabatic bulk
 548 moduli of capv (compared with that from the global experimental dataset, Extended Data Figure 7b), whilst the two
 549 AIMD studies^{4,5} predict a larger pressure effect on K_s than is observed in the experimental data. Other calculations
 550 employing mean-field and Landau theory³ suggest that shear softening should be associated with the cubic-tetragonal
 551 transition, whilst AIMD approaches do not include this behaviour^{4,5}. However, it has been proposed⁴ that the choice of
 552 cubic unit cell employed by Stixrude et al.³ prevented rotations of the SiO₆ octahedra, leading to an anomalously large
 553 shear modulus and explaining the high velocities. The AIMD results of Kawai and Tsuchiya⁴ should be preferred to those
 554 from Li et al.⁵, as the latter may not have fully converged and insufficiently sampled the Brillouin zone⁴ to accurately
 555 predict crystal structure. Despite differences, all three computational studies predict a larger shear modulus than required
 556 by experimental data (from both this and previous studies^{16,17}). It is possible that this discrepancy results from the strong
 557 anharmonicity of capv, implying that extremely expensive calculations may be required to accurately describe capv's
 558 elasticity using computational methods. Indeed, common first-principles methods inaccurately predict the elasticity or
 559 phonon temperature dependence of other anharmonic cubic perovskites (SrTiO₃, BaTiO₃ and PbTiO₃)⁵⁶⁻⁵⁸. Pseudopotentials
 560 that under/overestimate the cubic lattice parameter consistently over/underestimate the shear modulus in the opposite
 561 sense⁵⁶⁻⁵⁸. The Local-density-approximation (LDA), used by Kawai and Tsuchiya⁴, has been observed to overestimate the
 562 shear modulus (c_{44}) of SrTiO₃, BaTiO₃ and PbTiO₃ by 8-18 % for ~ 1% underestimate of unit cell volume⁵⁶. Since we observe
 563 a similar mismatch between the volume of cubic CaSiO₃ at adiabatic conditions based on our fit to experimental data and
 564 the results of Kawai and Tsuchiya⁴, which are ~ 1 % too small, we expect that capv's velocities predicted by Kawai and
 565 Tsuchiya⁴ will be somewhat overestimated. However, it is unlikely this effect can explain the entirety of the disagreement
 566 between previous calculations and our experimental results. A second contributor to the mismatch could be the presence
 567 of crystallographic preferred orientation (CPO) within experimental samples, especially if alignment of an acoustically slow
 568 direction coincided with the ultrasonic path. However, since refinement of X-ray diffraction patterns did not require CPO in
 569 the cubic CaSiO₃ field to fit the data, this seems unlikely. Additionally, the way crystal symmetry is stipulated and the lack of
 570 grain boundaries/defects in calculations may frustrate some phonon modes, further explaining the offset from
 571 experimental values. Finally, we re-iterate that the finite-strain model we report in this paper is subject to very large
 572 extrapolation from the experimental *PT* conditions (~ 12 GPa, 300 – 1500K) to those of the mantle (< 130 GPa, 1500 – 3000
 573 K) and we acknowledge additional experiments are now required to investigate in better detail the changes of capv velocity
 574 at more extreme conditions.

- 575 34. Guignard, J. & Crichton, W. A. The large volume press facility at ID06 beamline of the European synchrotron
576 radiation facility as a high pressure-high temperature deformation apparatus. *Rev. Sci. Instr.* **86**, 085112–11 (2015).
- 577 35. Hammersley, A. P. FIT2D: an introduction and overview, Technical Report ESRF-97-HA-02T. (1997).
- 578 36. Larson, A. C. & Dreele, Von, R. B. General structure analysis system (GSAS). 86–748 (1994).
- 579 37. Dorogokupets, P. I., Dewaele, A. & Dewaele, A. Equations of state of MgO, Au, Pt, NaCl-B1, and NaCl-B2: Internally
580 consistent high-temperature pressure scales. *High Pressure Research* **27**, 431–446 (2007).
- 581 38. Glazer, A. M. The classification of tilted octahedra in perovskites. *Acta Crystallographica Section B Structural
582 Crystallography and Crystal Chemistry* **28**, 3384–3392 (1972).
- 583 39. Woodward, P. M. Octahedral tilting in perovskites. I. Geometrical considerations. *Acta Cryst Sect A Found Cryst* **53**,
584 32–43 (1997).
- 585 40. Wood, I. G., Price, G. D., Street, J. N. & Knight, K. S. *Equation of State & Structural Phase Transitions in CaTiO₃
586 Perovskite. ISIS Experimental Report* (1997).
- 587 41. Kresse, G. & Furthmüller, J. Efficient iterative schemes for *ab initio* total-energy calculations using a plane-wave
588 basis set. *Phys. Rev. B* **54**, 11169–11186 (1996).
- 589 42. Kresse, G. & Joubert, D. From ultrasoft pseudopotentials to the projector augmented-wave method. *Phys. Rev B*
590 **59**, 1758–1775 (1999).
- 591 43. Perdew, J. P. *et al.* Restoring the density-gradient expansion for exchange in solids and surfaces. *Phys. Rev. Lett.*
592 **100**, 136406 (2008).
- 593 44. Togo, A. & Tanaka, I. First principles phonon calculations in materials science. *Scripta Materialia* **108**, 1–5 (2015).
- 594 45. Shim, S.-H., Duffy, T. S. & Shen, G. The stability and P-V-T equation of state of CaSiO₃ perovskite in the Earth's lower
595 mantle. *JGR* **105**, 25955–25968 (2000).
- 596 46. Sun, N. *et al.* Confirming a pyrolitic lower mantle using self-consistent pressure scales and new constraints on
597 CaSiO₃ perovskite. *JGR* (2016). doi:10.1002/2016JB013062
- 598 47. Wang, Y., Weidner, D. J. & Guyot, F. Thermal equation of state of CaSiO₃ perovskite. *JGR* **101**, 661–672 (1996).
- 599 48. Noguchi, M., Komabayashi, T., Hirose, K. & Ohishi, Y. High-temperature compression experiments of CaSiO₃
600 perovskite to lowermost mantle conditions and its thermal equation of state. *PCM* **40**, 81–91 (2013).
- 601 49. Chust, T. C., Steinle-Neumann, G., Dolejš, D., Schuberth, B. S. A. & Bunge, H. P. MMA-EoS: A computational
602 framework for mineralogical thermodynamics. *JGR* **122**, 9881–9920 (2017).
- 603 50. Brown, J. M. & Shankland, T. J. Thermodynamic parameters in the Earth as determined from seismic profiles.
604 *Geophysical Journal of the Royal Astronomical Society* **66**, 579–596 (1981).
- 605 51. Zhang, Z., Stixrude, L. & Brodholt, J. Elastic properties of MgSiO₃-perovskite under lower mantle conditions and the
606 composition of the deep Earth. *Earth Planet Sci Lett* **379**, 1–12 (2013).
- 607 52. Wentzcovitch, R. M. *et al.* Anomalous compressibility of ferropericlase throughout the iron spin cross-over.
608 *Proceedings of the National Academy of Sciences* **106**, 8447–8452 (2009).
- 609 53. Badro, J. *et al.* Electronic transitions in perovskite: Possible non-convecting layers in the lower mantle. *Science* **305**,
610 383–386 (2004).
- 611 54. Andrault, D., Fiquet, G., Guyot, F. & Hanfland, M. Pressure-induced Landau-type transition in stishovite. *Science*
612 **282**, 720–724 (1998).
- 613 55. Hernlund, J., Leinenweber, K., Locke, D. & Tyburczy, J. A. A numerical model for steady-state temperature
614 distributions in solid-medium high-pressure cell assemblies. *Am. Min.* **91**, 295–305 (2006).
- 615 56. Piskunov, S., Heifets, E., Eglitis, R. I. & Borstel, G. Bulk properties and electronic structure of SrTiO₃, BaTiO₃, PbTiO₃
616 perovskites: an *ab initio* HF/DFT study. *Computational Materials Science* **29**, 165–178 (2004).
- 617 57. Tadano, T. & Tsuneyuki, S. Self-consistent phonon calculations of lattice dynamical properties in cubic SrTiO₃ with
618 first-principles anharmonic force constants. *Phys. Rev. B* **92**, 054301 (2015).
- 619 58. Hachemi, A., Hachemi, H., Ferhat-Hamida, A. & Louail, L. Elasticity of SrTiO₃ perovskite under high pressure in cubic,
620 tetragonal and orthorhombic phases. *Physica Scripta* **82**, 025602 (2010).
- 621 59. Caracas, R., Wentzcovitch, R., Price, G. D. & Brodholt, J. CaSiO₃ perovskite at lower mantle pressures. *GRL* **32**,
622 L06306 (2005).
- 623 60. Jung, D. Y. & Oganov, A. R. *Ab initio* study of the high-pressure behavior of CaSiO₃ perovskite. *PCM* **32**, 146–153
624 (2005).
- 625 61. Mao, H. K. *et al.* Stability and equation of state of CaSiO₃-Perovskite to 134 GPa. *JGR* **94**, 17889–17894 (1989).
- 626 62. Yagi, T., Tsuchida, Y., Kusanagi, S. & Fukai, Y. Isothermal compression and stability of perovskite-type CaSiO₃.
627 *Proceedings of the Japan Academy Series B: Physical and Biological Sciences* **65**, 129–132 (1989).
- 628 63. Tamai, H. & Yagi, T. High-pressure and high-temperature phase relations in CaSiO₃ and CaMgSi₂O₆ and elasticity of
629 perovskite-type CaSiO₃. *PEPI* **54**, 370–377 (1989).
- 630 64. Tarrida, M. & Richet, P. Equation of state of CaSiO₃ perovskite to 96 GPa. *GRL* **16**, 1351–1354 (1989).

631 Extended Data Figure 1: **Lattice and diffraction peak parameters for CaSiO₃ and Ca[Si_{0.6}Ti_{0.4}]O₃ perovskite.** Refined lattice
 632 parameters and pseudo-cubic unit cell volumes from (a) and (c) Ca[Si_{0.6}Ti_{0.4}]O₃ and (b) and (d) CaSiO₃ plotted as a
 633 function of experimental temperature. (e) Full-width-at-half-maximum (fwhm) of diffraction peaks of the CaSiO₃
 634 perovskite sample, normalised to the fwhm at high temperature, measured at 100 °C intervals in a separate
 635 experiment to that in Figure 2.

636 Extended Data Figure 2: **X-ray diffraction patterns from CaSiO₃ perovskite.** Stacked diffraction patterns of CaSiO₃
 637 perovskite at ~ 25, 100 and 200 °C. (a) full patterns, (b) and (c) are limited in 2θ range to allow indication of weak
 638 superlattice peaks. Diffraction patterns are coloured by temperature conditions (see legend). The positions of the
 639 diffraction peaks from the capv sample, MgO, NaCl and Au are indicated by markers – other small peaks are from
 640 boron epoxy and/or furnace components. Cubic capv peaks are labelled with indices, hkl , in bold. The diffraction
 641 patterns reveal the appearance of small superlattice reflections at $T = 373$ and 300 K at ~ 6.1° , 8.05° , 12.1° and
 642 13.2° 2θ (NB there is believed to be an additional superlattice reflection obscured at 10.5° 2θ) labelled with hkl
 643 indexed on the tetragonal ($I4/m$) unit cell and marked with gold stars.

644 Extended Data Figure 3: **Refined X-ray diffraction patterns from Ca[Si_{0.6}Ti_{0.4}]O₃ perovskite.** top to bottom – Rietveld
 645 refinements of Ca(Si_{0.6}Ti_{0.4})O₃ samples from (a) in $P2_1/c$ with LaB₆ calibrant and ambient pressure and 300 K. (b) in
 646 the tetragonal $I4/m$ structure (with other cell components) at 890 K and high pressure (~ 12 GPa) and (c) in $Fm\bar{3}m$
 647 at 1336 K and high pressure (12 GPa).

648 Extended Data Figure 4: **X-ray diffraction patterns from Ca[Si_{0.6}Ti_{0.4}]O₃ perovskite.** (a) Complete diffraction pattern of the
 649 Ca(Si_{0.6}Ti_{0.4})O₃ sample as a function of temperature at ~ 12 GPa, with diffraction intensity indicated by colour scaling.
 650 (b)-(h) magnified panels focussing on the temperature evolution of the 311, 222, 400, 422, 440, 620 and 444
 651 diffraction peaks (indexed using a cubic lattice with $a \sim 7.3$ Å), demonstrating the change in thermal expansivity
 652 between cubic and tetragonal/monoclinic structures, and allowing visual identification of the observed phase
 653 transitions.

654 Extended Data Figure 5: **Phase diagram of calcium perovskite throughout the mantle from *ab-initio* simulations and
 655 experiments.** Cubic-tetragonal transition extrapolated throughout the mantle based on *ab initio* (solid circles) and
 656 experimental (triangles) constraints from this study. Vertical error bars (1σ) and the grey envelope (80% confidence
 657 interval) represent the uncertainty in computational results from this study. A 1500 K mantle adiabat and cold slab
 658 temperature profile are plotted as red curves, with dashed red arrows indicating the warming occurring during slab
 659 stagnation at 700-1000 km depth. Results from previous experimental and computational studies are plotted as open
 660 symbols and grey curves respectively.

661 Extended Data Figure 6: **Equations of state for CaSiO₃ perovskite.** (a) *PV* EoS for tetragonal CaSiO₃ at 300 K, fitted to data
 662 from this study only (purple line) and combined with data from previous studies (thick black curve). Only data with large
 663 symbols, those that used pressure transmitting media, have been included in fitting the EoS. All small symbols are from
 664 experiments that did not employ a pressure-transmitting medium so have been excluded as volumes are expected to be
 665 affected by residual sample stress. Additionally, data from Wang et al. (1996)⁴⁷ were excluded as they used energy

666 dispersive diffraction in the large volume press, which can be subject to larger uncertainties in volume. Computational
667 equations of state for tetragonal capv are plotted as dashed curves for comparison.^{3,17,19,45,47,59-64} b) *PVT* EoS for cubic
668 CaSiO₃ perovskite at 298 K and along a 1600 K adiabat fitted to data from this and previous studies. Small, partially
669 transparent symbols, are literature data that were not included in the fitting, either due to falling below the
670 calculated slope of the cubic-tetragonal transition (Methods) or due to concerns about data accuracy. The inset
671 histogram shows the, approximately normal, distribution for the residuals for the fitted data compared with the
672 best fit model, demonstrating the lack of outliers.

673 Extended Data Figure 7: **Bulk sound velocity and bulk modulus of CaSiO₃ perovskite.** (a) Bulk sound velocity of capv
674 predicted from the EoS in this study along a 1600 K mantle adiabat and at 300 K, compared with results from
675 previous computational studies on a 1600 K adiabat, a fit to previously published *PVT* diffraction data, and PREM.
676 (b) The adiabatic bulk modulus of CaSiO₃ perovskite calculated at 300 K and along a 1600 K mantle adiabat using the
677 finite strain model from this study, compared with thermodynamic results in Stixrude et al.⁶ and previous high
678 temperature computational studies^{4,5}.

679 Extended Data Figure 8: **Exemplar radiographic image, ultrasonic data and schematic of the experimental cell design.** (a)
680 Example of synchrotron radiographic image used to measure sample length from Ca(Si_{0.6}Ti_{0.4})O₃ sample, (b) ultrasonic
681 signals from “runa” experiment of CaSiO₃ sample and (c) cross section of the experimental assembly (to scale) used in
682 ultrasonic experiments throughout this study.

683 Extended Data Figure 9: **Comparison of bulk sound velocity from diffraction and ultrasonic measurements.** Comparison of
684 bulk sound velocity calculated from *PVT* equations of state, fitted to literature diffraction data (solid curves) and only that
685 reported by Gréaux et al. (dashed curves), compared with bulk sound velocities calculated from ultrasonic measurements
686 via $V_{\text{bulk}} = (V_p^2 - 4/3V_s^2)^{0.5}$ for data from Gréaux (squares) and this study (circles). All curves and symbols are coloured for
687 temperature.

688

689

